Supporting Information (SI): Assembling Responsive Microgels at Responsive Lipid Membranes

M. Wang et al. 10.1073/pnas.XXXXXXXXXX

Materials and Methods

Synthesis of Thermoresponsive PNIPAM Particles. In a typical procedure, *N*-isopropylacrylamide (NIPAM, 10 g) monomer, *N*, *N*′-methylene-bisacrylamide (BIS, 0.683 g) crosslinker and fluorescein O-methacrylate (FMA, 10 mg dissolved in 10 mL of water) dye in water (420 mL) were added to a double-walled glass reactor coupled to a water circulation thermostat. The reactor was fitted with a reflux condenser, a mechanical stirrer, a septum and a nitrogen gas inlet. Under nitrogen and stirring the reaction mixture was heated to 60°C and stirred for 40 minutes before increasing the temperature to 80°C. Then 2, 2' azobis(2-methylpropionamidine) dihydrochloride (V50, 0.1005 g in 10 ml of water) initiator was added drop-wise. After 4 hours the reaction mixture was cooled to 40°C and passed through glass wool to remove particulate matter. Further purification was obtained by performing cycles of centrifugation, decantation and dispersion until a clear supernatant was obtained.

Particle Characterization.

Dynamic light scattering (DLS). DLS was carried out using a light scattering goniometer instrument from LS Instruments equipped with a He-Ne laser ($\lambda = 632.8\ nm$). The samples were diluted to 0.01 wt% preventing interaction effects and multiple scattering. The measurements were performed at a scattering angle of 45° for temperatures varying between 20°C and 50°C. The hydrodynamic radius was derived from a first order cumulant analysis. Each sample was allowed to equilibrate at the desired temperature for 30 min before data collection. The resulting swelling curve is displayed in Fig. S1A.

Electrophoretic measurements and effective charge determination. The particle electrophoretic mobility, μ, was determined with a Zetasizer Nano-Z (Malvern) in pure Milli-Q water. The dispersions were highly diluted (0.01 wt%) to avoid multiple scattering. The obtained results are summarized in Fig. S1B.

Characterisation of lipid phase transitions.

Differential scanning calorimetry (DSC). DSC measurements were carried out on a VP-DSC calorimeter (MicroCal, INC., Northampton, MA, USA) using a chamber pressure of 25 psi. To ensure that thermal equilibrium was reached

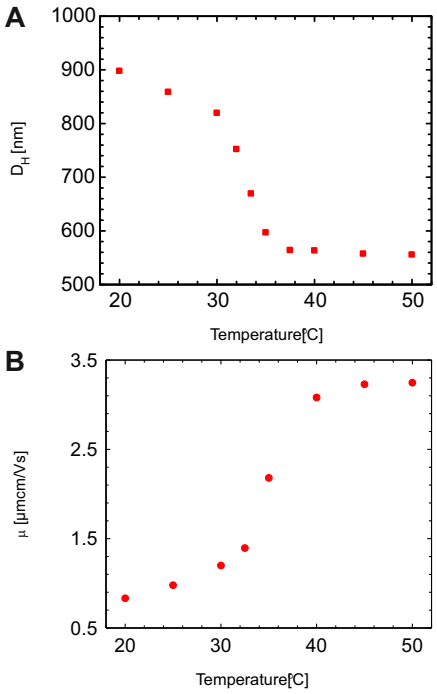

Fig. S1. (A) Temperature dependence of hydrodynamic diameter and (B) electrophoretic mobility of PNIPAM microgels.

and to check the reproducibility of the results, several scan cycles were recorded with up-scans from 5°C to 35°C at a scanning rate of 30°C/h. The samples were equilibrated at 5°C for 10 min before the experiment started. The transition temperatures and enthalpies of phase transitions were analyzed using the software Origin from MicroCal.

Stock solutions of the lipid mixtures used were prepared by dissolving the lipids in chloroform/methanol 90/10 (vol ratio). Smaller aliquots from the stock solutions were taken out and dried under a stream of air until the solvent was evaporated and a thin lipid film remained. The lipid film was suspended in water for at least 0.5 hour. The lipid dispersion was then vortexed to reach a dispersion of multilamellar vesicles. The total lipid concentration in the dispersion was 2 mM.

Adsorption at fluid bilayer: supporting information

Microgel@DOPC bilayer. In this section, we present the influence of the temperature on the distribution of the

particles at the DOPC bilayer quantified by the determination of their pair correlation function, $g(r)$, at the top of large GUVs shown in Fig. S2. Additional control experiments were performed with unlabelled vesicles to confirm that the adsorption process is not influenced by the dye present in the GUVs bilayer as illustrated in Fig. S3*A*. Finally in Fig. S3B, we demonstrate the partial reversibility of the assembly at the interface by imaging the decorated GUVs heated up at 40° after cooling down to 20°C.

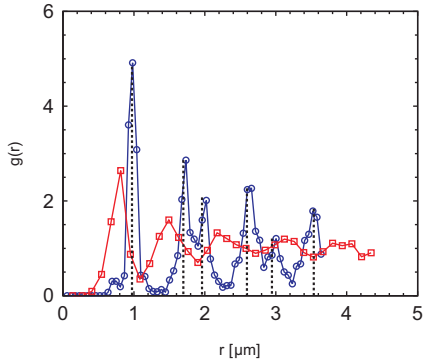

Fig. S2. Experimental in plane (2D) pair correlation function, $g(r)$, for the PNIPAM microgel crystals at DOPC GUV surface at 20°C (empty dots) and 30°C (empty squares). Dashed vertical lines (black) indicate the peaks of $g(r)$ of an ideal hexagonal packed monolayer generated numerically.

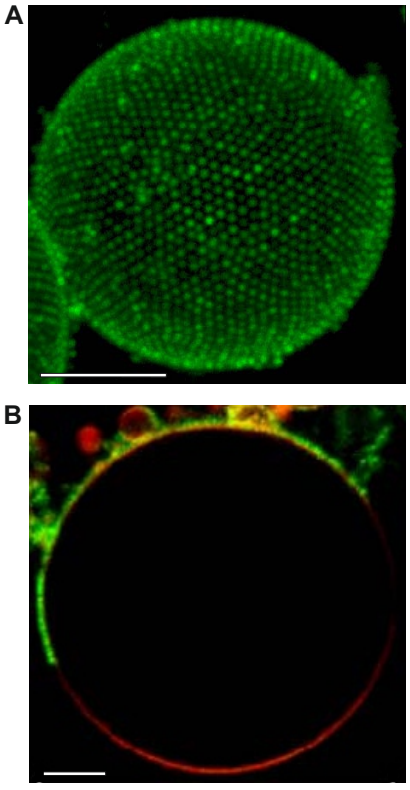

Fig. S3. (A) 3D confocal micrograph of DOPC GUV decorated with PNIPAM particles without Rhod-PE dye at 20°C. (B) Confocal micrograph of DOPC GUV decorated with PNIPAM microgel particles after decreasing the temperature from 40 to 20°C. Scale bars: 10 μm.

Microgel@DOPC/DOPE bilayer. We have investigated how particle adsorption and lateral organisation is affected by changes in bilayer composition through introducing a lipid with negative spontaneous curvature, DOPE. Experiments were performed with GUVs composed of DOPE/DOPC 20 : 80 (molar ratio) at 20°C (Fig. S4A). The results are strikingly similar to those obtained for the GUVs composed of only DOPC, showing 2D hexagonal lattice of particles with a average distance to the nearest neighbor determined from the $g(r)s$ to ca. 0.97 μm (Fig. S4B).

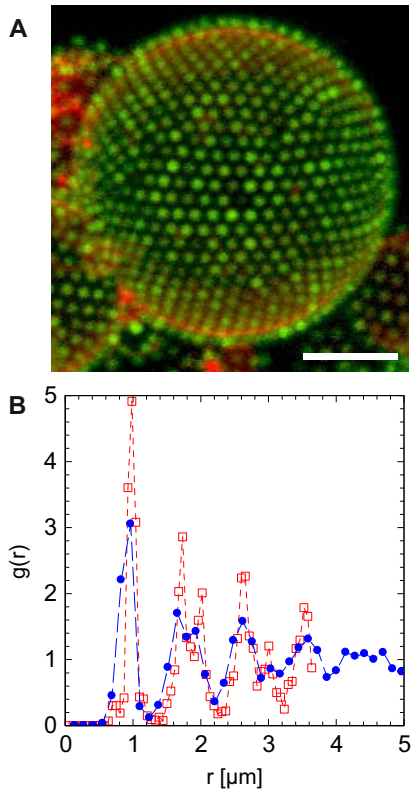

Fig. S4. (A) 3D reconstructions of the assembly showing the organization of the microgels in 2D hexagonal crystals at lipid bilayer composed of 20 : 80 DOPE/DOPC. Scale bar: 5 μm. (B) Pair-correlation function, $g(r)$ of PNIPAM particles adsorbed at 20°C at DOPC (empty squares) and at 20 : 80 DOPE-DOPC (solid dots) GUV.

Determination of the DMPC/DOPC phase diagram from calorimetric measurement

Fig. S5 shows the DSC heating curves for DMPC : DOPC mixtures at varying compositions. Pure DMPC in excess water exhibits two endothermic transitions on heating, a lower temperature lower enthalpy $L_\beta - P_\beta$ pre-transition at ca. 15°C and a higher temperature higher enthalpy $P_\beta - L_\alpha$ main transition (chain melting) at 24°C. Pure DOPC in excess water does not show any transition within the temperature range investigated. For the mixed lipid samples, the peak corresponding to the melting transition broadens and goes to lower temperatures, implying melting point depression and two phase co-existences.

The position of the phase boundaries in Fig. S5A are determined from the width of the broad enthalpy peak.

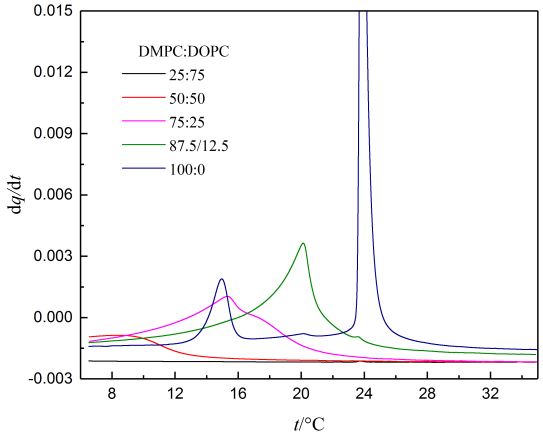

Fig. S5. DSC trace of the hydrated DMPC : DOPC mixture and pure DMPC at high water content.

Lipogel adsorption experiments on unlabeled GUVs

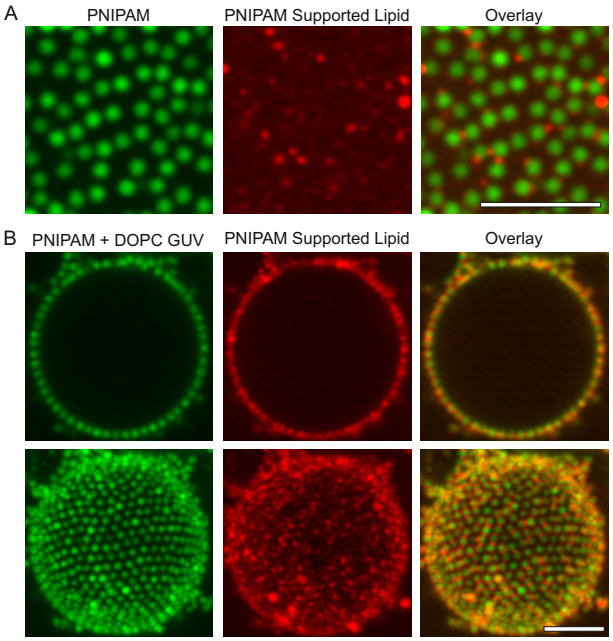

Fig. S6. (*A*) 2D CLSM micrographs of lipid-poor lipogels adsorbed at the glass coverslip. These particles contain five times less lipid compared to the experiments shown in Fig. 5. (*B*) 2D and 3D micrographs of NBD-PE labeled DOPC giant vesicles decorated with lipid-poor lipogels from left to right: green fluorescence of copolymerized FMA in PNIPAM microgels, red fluorescence of Rhod-PE present in the lipid coating of the microgels and overlay of the two channels. Temperature 20°C. Scale bars: 5 μm.

Additional experiments were performed on the adsorption of lipogels on unlabeled GUVs. Figure S6 presents the results obtained using a lipid poor lipogels, where the associated additional lipids were found to locally bridge neighboring microgels at the surface of the GUVs.

Microgel wrapping at lipid bilayers

In order to estimate the wrapping angle α, isolated particles were imaged at the central section of DOPC GUVs. The microgels are assumed as non-deformable particles with a size, R_P, provided by their hydrodynamic radius. The wrapping angle α is then determined from the position of the microgel and of the bilayer at contact as illustrated in Fig. S7*A*. During these measurements, we were not able to clearly resolve the contact area and the local bending of the bilayer. In addition, the low indentation of the bilayer makes the resolution of the local deformation challenging as the particle size are in the order of the optical thickness of the confocal microscope. Considering the resolution of our images with a pixel size of ≈ 50 nm, it would lead to an absolute error in the order of $\pm\ 12°$ on this measurement.

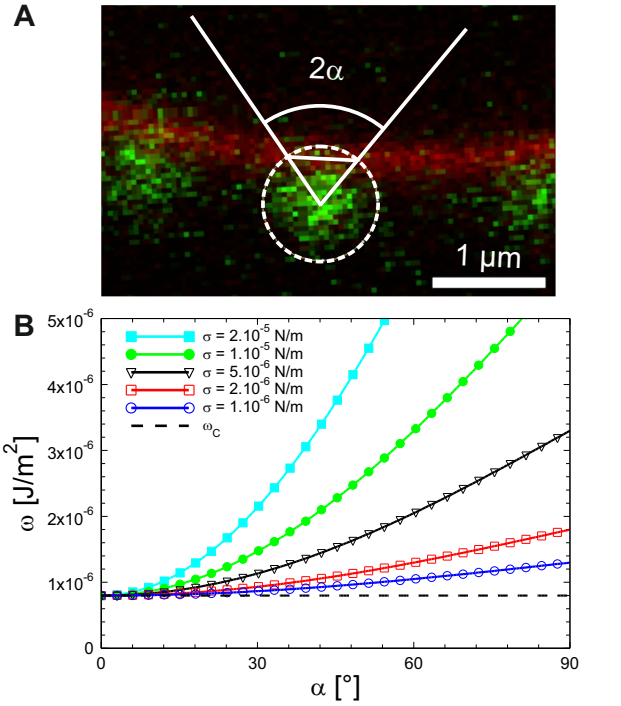

Fig. S7. (A) Early stage adsorption of the microgel at the surface of a DOPC bilayer at 20°C and geometrical construction for the determination of $\alpha \approx 37°$. (B) Estimation of the adhesion energy per unit area, ω, as function of α considering $R_P = 450$ nm, $\kappa = 20\ k_BT$ for $\sigma = 2 \times 10^{-5}$ N/m (solid squares), $\sigma = 10^{-5}$ N/m (solid dots), $\sigma = 5 \times 10^{-6}$ N/m (empty triangles), $\sigma = 5 \times 10^{-6}$ N/m (empty squares), $\sigma = 10^{-6}$ N/m (empty dots) and $\sigma = 0$ N/m (dashed line).

In Fig. S7*B*, the adhesion energy ω is calculated for different lateral tensions as a function of α using eq. 1 and 7 in the main manuscript. The dashed line refers to the critical value of adhesion energy for particle wrapping, ω_c. Next, we focus on the influence of α on R_P. Using eq. 7 in the main manuscript, α reads:

$$\alpha = cos^{-1}\left(1 + \frac{2}{\sigma}\left(\omega - \frac{2\kappa}{R_P^2}\right)\right). \qquad [1]$$

The calculations are summarized for $\omega = 3 \times 10^{-6}$ J/m^2 in

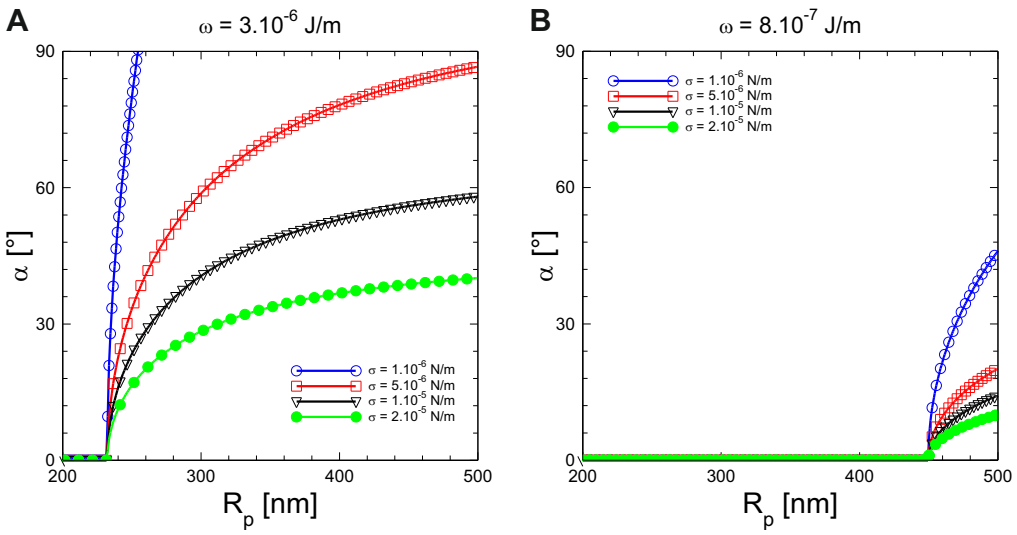

Fig. S8. Wrapping angle dependence on the microgel size at constant adhesion energy calculated for different lateral tensions for $\omega = 3\times10^{-6}$ J/m^2 (A) and $\omega = 8\times10^{-7}$ J/m^2 (B).

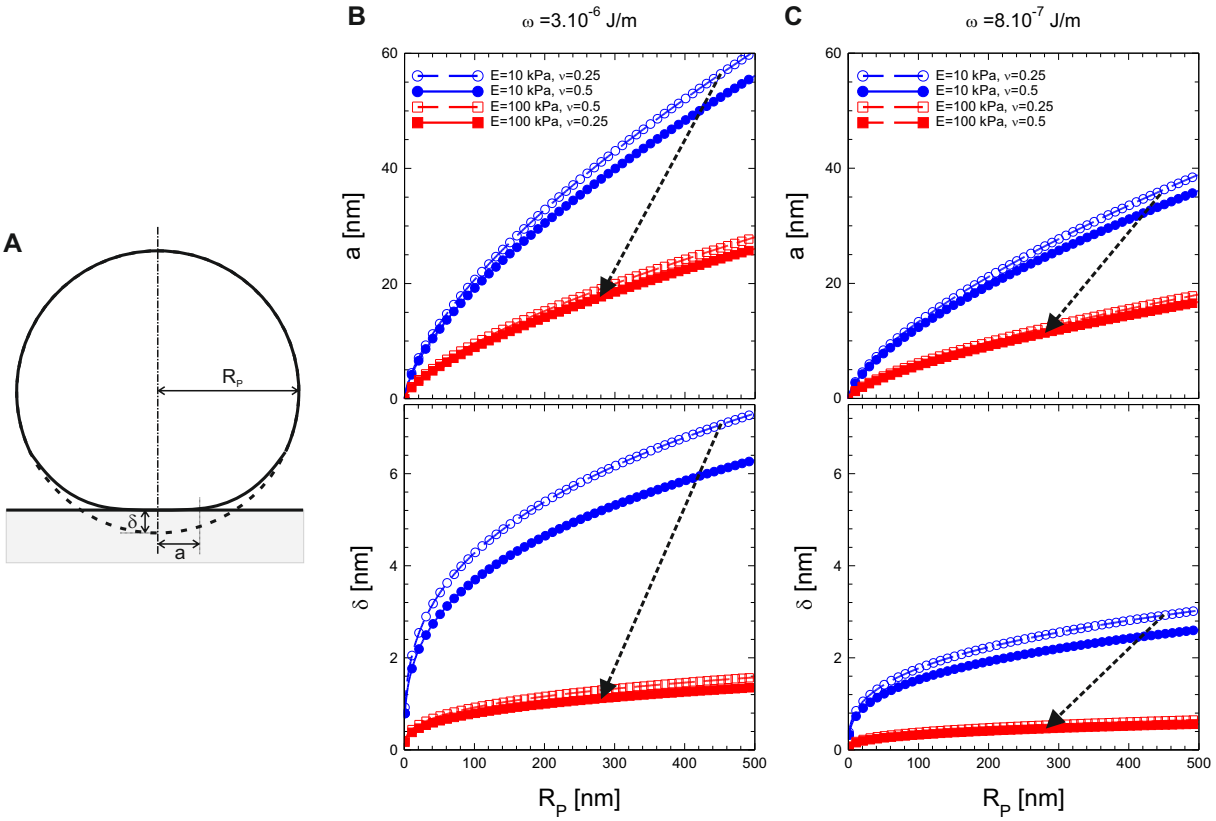

Fig. S9. (A) Schematic representation of an elastic particle with a size R_P at contact with a hard adhesive substrate following the Derjaguin adhesive contact model (1). Upon contact the contact area is defined by the radius a (top panels) and the penetration δ (bottom panels). (B, C) Calculations of a and δ for E=10 and 100 kPa and ν=0.25 and 0.5 for $\omega = 3\times10^{-6}$ J/m^2 (B) and $\omega = 3\times10^{-6}$ J/m^2 (C), respectively. The dashed arrows mark the transition from a swollen "soft" microgel to a collapsed "harder" microgel.

Fig. S8A and for $\omega = 8\times10^{-7}$ J/m^2 in Fig. S8B. Different σ-values are considered ranging from 10^{-6} to 2×10^{-5} N/m. The size dependence is more pronounced at lower σ-values. The minimum particle size for a particle to adsorb is here determined by κ and ω such that $R_P = (2\kappa/\omega)^{0.5}$.

Derjaguin adhesive contact calculation

Considering the microgels as soft particles, we employed the Derjaguin model for adhesive contact to determine the contact area, a, and the penetration depth, δ using eq. 8 and 9 in the main manuscript. A schematic representation

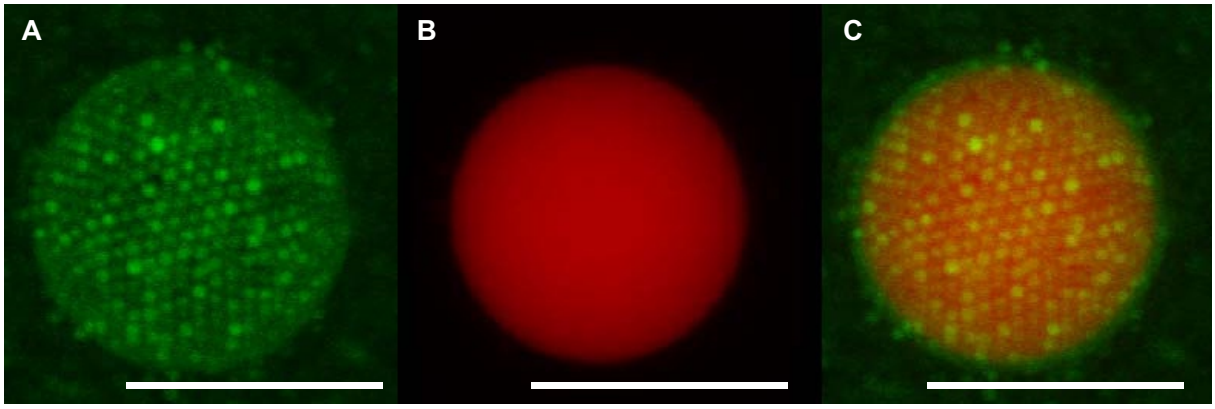

Fig. S10. Fluorescence CLSM 3D reconstruction of a pyrromethene-stained silicon oil droplet decorated with 2D hexagonal crystals of microgels. The oil droplet is stained with pyrromethene 546. (A) and (B) show green and red fluorescence, respectively, recorded in sequential mode, whereas in (C) red and green fluorescences are combined. Scale bars: 10 μm.

of a particle adsorbed at a solid interface is shown in Fig. S9A. The elastic modulus of microgel, E, is typically in the order of 10- 100 kPa. In addition, above T_{VPT} it increases by about an order of magnitude. The volume phase transition is accompanied by a an increase of the Poisson ratio, ν from ≈ 0.25 to 0.5 from a swollen to collapse configuration of the microgels. Therefor, we consider $E = 10$ kPa, $\nu = 0.25$ for "soft" microgels and $E = 100$ kPa, $\nu = 0.5$ for "harder" microgels. Figure S9 presents the different calculation of a and δ performed for the different E- and ν- values calculated as a function of R_P. Similarly to the former section, two ω-values are considered; $\omega = 3 \times 10^{-6}$ J/m^2 in Fig. S9A and $\omega = 8 \times 10^{-7}$ J/m^2 in Fig. S9B. The dashed arrows indicate changes occurring from the swollen configuration, i. e., soft microgel with $R_P = 450$ nm, to the collapsed configuration, i. e., harder microgel with $R_P = 280$ nm. The local deformation can be estimated combining eq. 8 and 9 following:

$$\frac{\delta}{R_P} = \frac{a^2}{R_P^2} \approx \left(\frac{\pi\omega(1-\nu^2)}{R_p E} \right)^{\frac{2}{3}}. \qquad [2]$$

Adsorption of microgels to oil droplets: microgel stabilized emulsion

In order to investigate the microgels ability to adapt their conformation at a fluid interfaces, we prepared a microgel stabilized emulsion by vortexing low-viscosity silicon oil in water in the presence of an excess of microgels to ensure sufficient decoration of the oil droplets (2). Fig. S10 shows the CLSM 3D reconstruction of the microgels densely pack at the interface into a well-ordered 2D hexagonal array. We estimate the average microgel centre-to-centre distance at 0.72 μm. If we compared this value with the apparent hydrodynamic diameter in bulk, 0.90 μm, the dense packing of the microgels reflects their soft repulsive potential which allows for an significant overlap at the oil droplet interface. This behavior has been previously observed for Pickering microgels emulsions as described in reference (2). Also here, we do not observe any flattering or fried egg-like conformation of adsorbed microgels as often reported in the literature (3, 4). Instead, the microgels appear to compress and/or to interpenetrate at the interface as previously described (2).

Simplified model of the interparticle interaction of large undeformable particles wrapped at tense lipid bilayers

Adsorbing particles results in the local displacement of the lipid and to an additional tension that has to be dissipated by the free bilayer. The latter can be expressed as in eq. 5 by

$$E_{ten,free} = \pi R_F^2 z^2 \sigma, \qquad [3]$$

where R_F defines the mean curvature of the free bilayer. In our model the distance between the centers of two adsorbed particles, r is given by:

$$r = 2(R_P + R_F) sin\alpha. \qquad [4]$$

As schematically depicted in Fig. S9A, the tension within the bilayer has relaxed when $E_{ten,ad} = E_{ten,free}$. This condition is then fulfilled when $r = r_{max}$ such that

$$r_{max} = 4R_P sin\alpha. \qquad [5]$$

When $r > r_{max}$, there is no extra work (Fig. S11B), whereas for $r < r_{max}$ (Fig. S11C) an excess tension is generated setting a net repulsive potential between two approaching particles. This potential, defined as U_{ten} is given by the difference of tension energies $U_{ten} = E_{ten,ad} - E_{ten,free}$ following:

$$\begin{aligned} U_{ten} &= \pi\sigma z^2 \left(\frac{r^2 - 4rR_P sin\alpha}{4sin^2\alpha} \right), \quad when \quad r \leq r_{max} \\ &= 0, \quad when \quad r > r_{max} \end{aligned} \qquad [6]$$

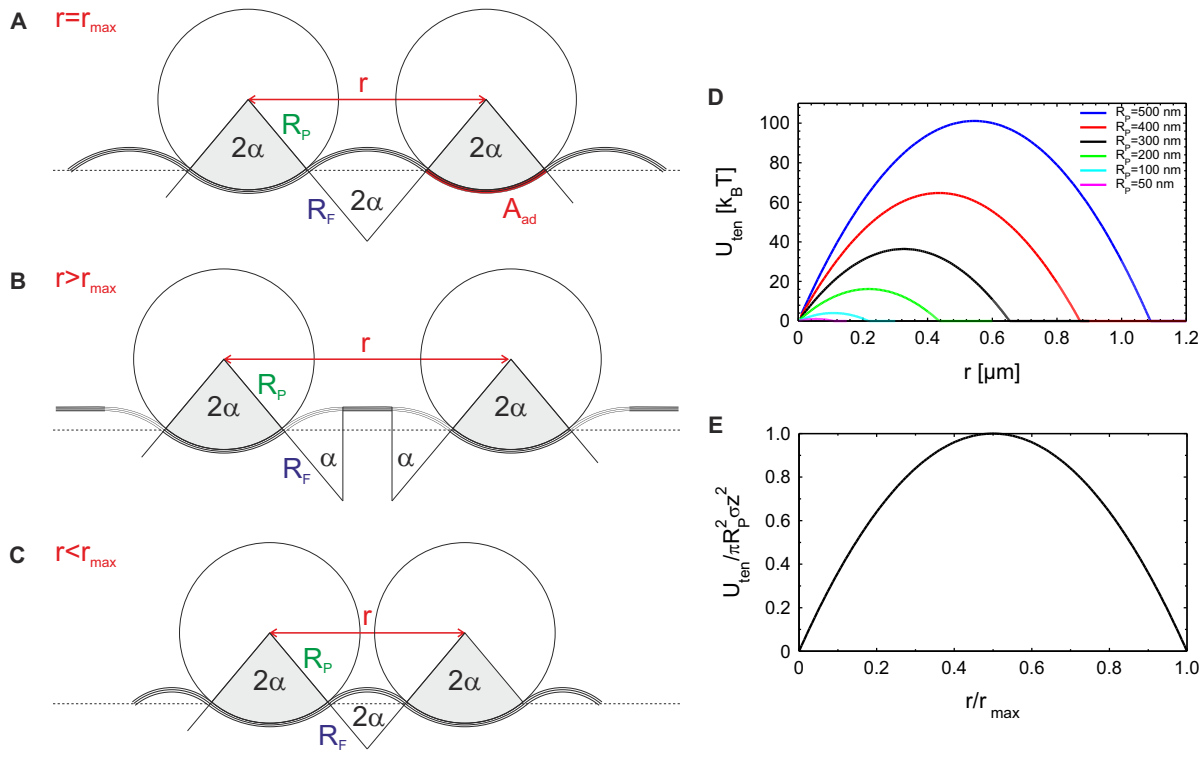

Fig. S11. (A-C) Schematic representation of particles partially wrapped at the surface of a flat bilayer at different interparticle distance. (D) Calculation of the interaction potential, U_{ten}, generated by the tension within the bilayer calculated for $R_P = 500$ nm, $\sigma = 5 \times 10^{-5}$ J/m and $\alpha = 33°$. (E) Dimensionless representation of U_{ten} as function of r/r_{max}.

U_{ten} is plotted in Fig. S11D for different R_P-values. a general dimensionless form is obtained by expressing U_{ten} normalized by $A_{ad}\sigma z^2$ as a function of a reduced interparticle distance defined as $r/r_{max} = r/(4R_P sin\alpha)$ (Fig. S11E).

$$\frac{U_{ten}}{\pi R_P^2 \sigma z^2} = 4\left(\left(\frac{r}{r_{max}}\right)^2 - \left(\frac{r}{r_{max}}\right)\right) \qquad [7]$$

In our experiments, we found that $r_{max} \approx 2.2R_P$ considering that R_P corresponds to the hydrodynamic radius of the particles. By plugging this value into eq. 11, one obtains $\alpha \approx 33°$. This value is in good agreement with our rough estimate of the degree of wrapping shown in Fig. S8A, which corresponds to $\alpha \approx 37 \pm 5°$. This simple model implies that the particles do not interact for $r \geq r_{max}$, whereas for $r < r_{max}$ a net repulsion is to be expected from the tension generated within the bilayer. It is worthwhile noting that our model further indicate that the particles will be at contact for $\alpha = 30°$. For lower α-value, r_{max} becomes sensitive to the interparticle interaction potential and corresponds to the balance between the attraction generated by the bilayer tension energy and the repulsive interparticle interaction. Our results thus suggests that for low degree of wrapping, the organization of the short-range repulsive particles into crystals and the corresponding lattice parameter allows for the determination of the degree of wrapping and ultimately for known bilayer κ- and σ-values to estimate the adhesion energy between particle and bilayer. Following this model, it is as well interesting to note that the separation between the particles should increase for larger α-values such that for $\alpha = 90°$, $r_{max} = 2r_p$. We reiterate that this schematic model is considered for large particles adsorbed on large tense GUVs. For smaller particles and more rigid bilayers, it should include the contribution of the bending energy. In addition, for simplicity it neglects the multibody interactions as well as the more complex 3D topology of the deformed bilayer. It therefore mostly aims at describing the interactions at play and their order of magnitude.

Supplementary Videos

Video S1: Video showing the adsorption and diffusion process of PNIPAM microgel particles on the outside surface of the DOPC GUV at 20°C.

Video S2: Combined time series showing the mobility of PNIPAM particles adsorbed at the surface of DMPC GUVs at 17°C and 30°C.

References

1. Derjaguin BV (1934) Untersuchungen über die reibung und adhäsion. *Kolloid Z.* 69:155–164.

2. Månsson LK, Immink JN, Mihut AM, Schurtenberger P, Crassous JJ (2015) A new route towards colloidal molecules with externally tunable interaction sites. *Faraday Discuss.* 181:49–69.
3. Destribats M, et al. (2011) Soft microgels as pickering emulsion stabilisers: role of particle deformability. *Soft Matter* 7(17):7689–7698.
4. Destribats M, et al. (2014) Impact of pnipam microgel size on its ability to stabilize pickering emulsions. *Langmuir* 30:1768–1777.